Bayesian analysis of the break in *DAMPE* lepton spectra

Jia-Shu Niu,[1,2,*] Tianjun Li,[1,2,†] Ran Ding,[3] Bin Zhu,[4] Hui-Fang Xue,[5] and Yang Wang[6]

[1]*CAS Key Laboratory of Theoretical Physics, Institute of Theoretical Physics, Chinese Academy of Sciences, Beijing 100190, China*

[2]*School of Physical Sciences, University of Chinese Academy of Sciences, No. 19A Yuquan Road, Beijing 100049, China*

[3]*Center for High-Energy Physics, Peking University, Beijing 100871, People's Republic of China*

[4]*Department of Physics, Yantai University, Yantai 264005, People's Republic of China*

[5]*Astronomy Department, Beijing Normal University, Beijing 100875, People's Republic of China*

[6]*School of Mathematical Sciences, Shanxi University, Shanxi 030006, People's Republic of China*

(Received 9 January 2018; published 26 April 2018)

Recently, *DAMPE* has released its first results on the high-energy cosmic-ray electrons and positrons (CREs) from about 25 GeV to 4.6 TeV, which directly detect a break at ∼1 TeV. This result gives us an excellent opportunity to study the source of the CREs excess. In this work, we used the data for proton and helium flux (from AMS-02 and CREAM), $\bar{p}/p$ ratio (from AMS-02), positron flux (from AMS-02) and CREs flux (from *DAMPE* without the peak signal point at ∼1.4 TeV) to do global fitting simultaneously, which can account for the influence from the propagation model, the nuclei and electron primary source injection, and the secondary lepton production precisely. For an extra source to interpret the excess in lepton spectrum, we consider two separate scenarios (pulsar and dark matter annihilation via leptonic channels) to construct the bump ($\gtrsim$100 GeV) and the break at ∼1 TeV. The result shows that (i) in the pulsar scenario, the spectral index of the injection should be $\nu_{\rm psr} \sim 0.65$ and the cut-off should be $R_c \sim 650$ GV; (ii) in dark matter scenario, the dark matter particle's mass is $m_\chi \sim 1208$ GeV, and the cross section is $\langle \sigma v \rangle \sim 1.48 \times 10^{-23}$ cm^3 s^{-1}. Moreover, in the dark matter scenario, the $\tau\bar{\tau}$ annihilation channel is highly suppressed, and a DM model is built to satisfy the fitting results.

DOI: 10.1103/PhysRevD.97.083012

I. INTRODUCTION

Recently, the *DAMPE* (DArk Matter Particle Explorer) [1,2] satellite, which was launched on December 17, 2015, released its first data on high-energy cosmic-ray electrons and positrons (CREs) [3]. *DAMPE* has measured the CRE (i.e., $e^- + e^+$) spectrum in the range of 25 GeV–4.6 TeV with unprecedented energy resolution (better than 1.2% $\gtrsim$100 GeV). The results show a bump at about 100 GeV–1 TeV, which is consistent with previous results [4–9]. More interesting, a break at ∼1 TeV and a peak signal at ∼1.4 TeV have been detected. All of these features cannot be described by a single power law and provide us with an opportunity to study the source of high-energy CREs.

The peak signal at ∼1.4 TeV has been studied by many works which employed nearby pulsar winds, supernova remnants (SNRs), and dark matter (DM) substructures [10–24]. At the same time, considering the statistical confidence level of this signal is about 3σ which needs more counts in the future, we exclude the peak signal and do a global fitting on the left points in the *DAMPE* CRE spectrum in this work. As a result, if we refer to the *DAMPE* CRE flux in this work, the peak point is excluded except for special emphasis.

In cosmic ray (CR) theory, the CR electrons are expected to be accelerated during the acceleration of CR nuclei at the sources, e.g., SNRs, but the CR positrons are produced as secondary particles from CR nuclei interaction with the interstellar medium (ISM) [4,25–27]. From the results of the flux of positrons and electrons [6,28–30], we can infer that there should be some extra sources producing electron-positron pairs. This can be interpreted both by the astrophysical sources' injection [14,31–37] and DM annihilation or decay [38–44].

As a result, the CRE data contain the primary electrons, the secondary electrons, the secondary positrons, and the extra source of electron-positron pairs. If we want to study the properties of the extra source, we should deduct the primary electrons and secondary electrons/positrons first. The primary electrons are always assumed to have a power-law form injection, and the secondary electrons/positrons are determined dominatingly by the CR proton and helium particles interacting with ISM. Consequently, we should complete global fitting to these data simultaneously, which can avoid the bias of choosing the lepton background parameters.

*jsniu@itp.ac.cn
†tli@itp.ac.cn

Considering the situations of the high-dimensional parameter space of the propagation model and precise data sets, we employ a Markov chain Monte Carlo (MCMC [45]) method (embedded by DRAGON) to achieve global fitting and sample the parameter space of all the related parameters to reproduce the CRE spectrum [46–49].

Moreover, because of the significant difference in the slopes of proton and helium, of ∼0.1 [50–54], that has been observed, we use separate primary source spectra settings for the proton and helium. Note also that we consider propagation of nuclei only up to $Z = 2$ and neglect possible contributions from the fragmentation of $Z > 2$ nuclei, which should be a good approximation since their fluxes are much lower than the p and He fluxes [55]. In this condition, all the secondary particles (antiprotons and leptons) are produced from the interactions among the proton, helium, and ISM, which give us a self-consistent way to combine the nuclei and lepton data together.

This paper is organized as follows. We first introduce the setups of our work in Sec. II. The global fitting method and the chosen data sets and parameters are given in Sec. III. After presenting the fitting results and discussions in Sec. IV, we summarize our results in Sec. V.

II. SETUPS

In this section, we list some of the most important setups in this work which are different from our previous work [49]. More detailed descriptions can be found in Ref. [49].

A. Propagation model

In this work, we use the diffusion-reacceleration model which is widely used and can give consistent fitting results to the AMS-02 nuclei data (see, e.g., [48,49]). A uniform diffusion coefficient $[D_{xx} = D_0\beta(R/R_0)^{\delta}]$ is used in the whole propagation region.

At the same time, because high-energy CREs lose energy due to processes like inverse Compton scattering and synchrotron radiation, we parametrize the interstellar magnetic field in cylinder coordinates (r, z) as

$$B(r,z) = B_0 \exp\left(-\frac{r - r_\odot}{r_B}\right) \exp\left(-\frac{|z|}{z_B}\right), \quad (1)$$

to calculate the energy loss rate. In Eq. (1), $B_0 = 5 \times 10^{-10}$Tesla, $r_B = 10$ kpc, and $z_B = 2$ kpc [56], and $r_\odot \approx 8.5$ kpc is the distance from the Sun to the galactic center.

B. Primary sources

In this work, considering the fine structure of spectral hardening for primary nuclei at ∼300 GeV (which was observed by ATIC-2 [50], CREAM [51], PAMELA [52], and AMS-02 [53,54]) and the observed significant difference in the slopes of proton and helium (of about ∼0.1 [53,54,57]), we use separate primary source spectra settings for proton and helium, and each of them has 2 breaks at rigidity R_{A1} and R_{A2}. The corresponding slopes are ν_{A1} $(R \le R_{A1})$, ν_{A2} $(R_{A1} < R \le R_{A2})$, and ν_{A3} $(R > R_{A3})$. For cosmic-ray electrons' primary source, we followed the same configuration as those for proton and helium, but due to the *DAMPE* lepton data range (20 GeV–4 TeV), we use 1 break R_e for the electron primary source, and the corresponding slopes are ν_{e1} $(R \le R_e)$ and ν_{e2} $(R > R_e)$.

C. Secondary sources

The secondary cosmic-ray particles are produced in collisions of primary cosmic-ray particles with ISM. The secondary antiprotons are generated dominantly from inelastic pp collisions and pHe collisions. At the same time, the secondary electrons and positrons are the final product of decay of charged pions and kaons, which were in turn mainly created in collisions of primary particles with gas. As a result, the corresponding source term of secondary particles can be expressed as

$$q_{\rm sec} = \frac{c}{4\pi} \sum_{i={\rm H,He}} n_i \sum_j \int {\rm d}p' \beta n_j(p') \frac{{\rm d}\sigma_{i,j}(p,p')}{{\rm d}p}, \quad (2)$$

where n_i is the number density of interstellar hydrogen (helium), ${\rm d}\sigma_{i,j}(p,p')/{\rm d}p$ is the differential production cross section, $n_j(p')$ is the CR species density, and p' is the total momentum of a particle.

To partially take into account the uncertainties when calculating the secondary fluxes, we employ parameters $c_{\bar{\rm p}}$ and c_{e^+} to rescale the calculated secondary flux to fit the data [47,58–61]. Note that the above mentioned uncertainties may not be simply represented with a constant factor but that most probably they are energy dependent [62,63]. Here, we expect that a constant factor is a simple assumption.

D. Extra sources

In this work, two kinds of extra lepton sources are considered. The pulsar scenario account for the extra lepton source to the pulsar ensemble in our galaxy, which is able to generate high-energy positron-electron pairs from their magnetosphere. The injection spectrum of the CREs in such a configuration can be parametrized as a power law with an exponential cutoff:

$$q_e^{\rm psr}(p) = N_{\rm psr}(R/10\ {\rm GeV})^{-\nu_{\rm psr}} \exp(-R/R_{\rm c}), \quad (3)$$

where $N_{\rm psr}$ is the normalization factor, $\nu_{\rm psr}$ is the spectral index, $R_{\rm c}$ is the cutoff rigidity. The spatial distribution of this pulsar ensemble which provides continuous and stable CRE injection obeys the form in Eq. (5) in Ref. [49], with slightly different parameters: $a = 2.35$ and $b = 5.56$ [47].

The DM scenario ascribes the extra lepton source to the annihilation of Majorana DM particles distributed in our galaxy halo, whose source term always has the form

$$Q(\mathbf{r}, p) = \frac{\rho(\mathbf{r})^2}{2m_\chi^2}\langle\sigma v\rangle\sum_f \eta_f \frac{dN^{(f)}}{dp}, \tag{4}$$

where $\rho(\mathbf{r})$ presents the DM density distribution, $\langle\sigma v\rangle$ is the velocity-averaged DM annihilation cross section multiplied by DM relative velocity, and $dN^{(f)}/dp$ is the injection energy spectrum of CREs from DM annihilating into standard model (SM) final states through all possible channels f with η_f (the corresponding branching fractions). In this work, we considered DM annihilation via leptonic channels, and the corresponding branching fractions for e^-e^+, $\mu\bar{\mu}$, and $\tau\bar{\tau}$ are η_e, η_μ, and η_τ, respectively ($\eta_e + \eta_\mu + \eta_\tau = 1$). We use the results from Ref. [64], which includes the electroweak corrections [65], to calculate the electron (positron) spectrum from DM annihilation by different channels. At the same time, we use the Einastro profile [66–69] to describe the DM spatial distribution in our galaxy, which has the form

$$\rho(r) = \rho_\odot \exp\left[-\left(\frac{2}{\alpha}\right)\left(\frac{r^\alpha - r_\odot^\alpha}{r_s^\alpha}\right)\right], \tag{5}$$

with $\alpha \approx 0.17$ and $r_s \approx 20$ kpc, and $\rho_\odot \approx 0.39$ GeV cm^{-3} is the local DM energy density [70–74].

E. Solar modulation

We adopt the force-field approximation [75] to describe the effects of solar wind and heliosperic magnetic field in the solar system, which contains only one parameter, the so-called solar modulation ϕ. Considering the charge-sign dependence solar modulation represented in the previous fitting [49], we use $\phi_{\rm nuc}$ for nuclei (proton and helium) data and $\phi_{\bar{\rm p}}$ for $\bar{\rm p}$ data to do the solar modulation. At the same time, we use ϕ_{e^+} to modulate the positron flux. Because the *DAMPE* lepton data $\gtrsim$20 GeV, we did not consider the modulation effects on electrons (or leptons).

F. Numerical tools

The public code DRAGON[1] [76] was used to solve the diffusion equation numerically because of its good performance on clusters. Some custom modifications are performed in the original code, such as the possibility to use species dependent injection spectra, which is not allowed by default in DRAGON.

In view of some discrepancies when fitting with the new data which use the default abundance in DRAGON [77], we use a factor $c_{\rm He}$ to rescale the helium-4 abundance (which has a default value of 7.199×10^4) which help us to get a global best fitting.

The radial and z grid steps are chosen as $\Delta r = 1$ kpc, and $\Delta z = 0.5$ kpc. The grid in kinetic energy per nucleon is logarithmic between 0.1 GeV and 220 TeV with a step factor of 1.2. The free escape boundary conditions are used by imposing ψ equal to zero outside the region sampled by the grid.

III. FITTING PROCEDURE

A. Bayesian inference

As in our previous works [49], we take the prior probability distribution function (PDF) as a uniform distribution and the likelihood function as a Gaussian form. The algorithms such as the one by Goodman and Weare [78] instead of classical Metropolis-Hastings is used in this work for its excellent performance on clusters. The algorithm by Goodman and Weare [78] was slightly altered and implemented as the Python module EMCEE[2] by Foreman-Mackey *et al.* [79], which makes it easy to use because of the advantages of Python. Moreover, EMCEE could distribute the sampling on the multiple nodes of modern cluster or cloud computing environments and then increase the sampling efficiency observably.

B. Data sets and parameters

In our work, the proton flux (from AMS-02 and CREAM [51,53]), helium flux (from AMS-02 and CREAM [51,54]), and $\bar{\rm p}/{\rm p}$ ratio (from AMS-02 [80]) are added in the global fitting data set to determine not only the propagation parameters but also the primary source of nuclei injections which further produce the secondary leptons. The CREAM data were used as the supplement of the AMS-02 data because they are more compatible with the AMS-02 data when $R \gtrsim 1$ TeV. The errors used in our global fitting are the quadratic summation over statistical and systematic errors.

On the other hand, the AMS-02 positrons flux [30] is added to set calibration to the absolute positron flux in *DAMPE* CREs flux [3]. Although the electron energy range covered by AMS-02 is lower than TeV and there are systematics between the AMS-02 and *DAMPE* CREs data, fittings to the AMS-02 leptonic data provide a self-consistent picture for the extra source models. As the extra sources accounting for the AMS-02 results may provide contribution to the TeV scale, the AMS-02 data could also constrain the properties of the predicted $e^- + e^+$ spectrum above ~TeV. Considering the degeneracy between the different lepton data, we use the positron flux from AMS-02 and CREs flux from *DAMPE* together to constrain the extra source properties. The systematics are dealt with by employing a rescale factor c_{e^+} on positron flux.

[1] https://github.com/cosmicrays/DRAGON.

[2] http://dan.iel.fm/emcee/.

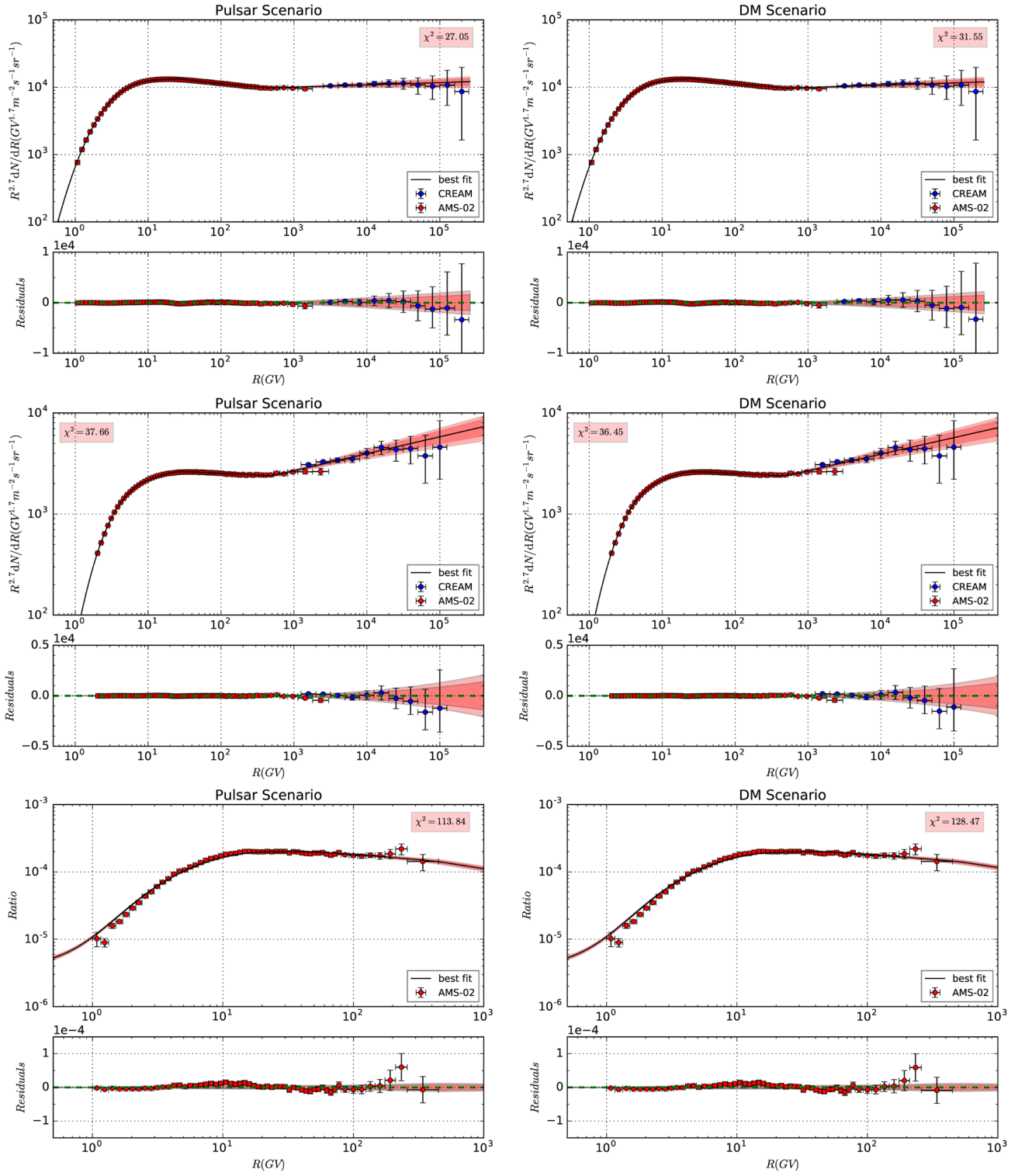

FIG. 1. Global fitting results and the corresponding residuals to the proton flux, helium flux, and $\bar{\mathrm{p}}/\mathrm{p}$ ratio for two scenarios. The 2σ (deep red) and 3σ (light red) bound are also shown.

Altogether, the data set in our global fitting is

$$D = \{D_{\mathrm{p}}^{\text{AMS-02}}, D_{\mathrm{He}}^{\text{AMS-02}}, D_{\bar{\mathrm{p}}/\mathrm{p}}^{\text{AMS-02}}, D_{\mathrm{p}}^{\text{CREAM}}, D_{\mathrm{He}}^{\text{CREAM}}, D_{e^+}^{\text{AMS-02}}, D_{e^-+e^+}^{\text{DAMPE}}\}.$$

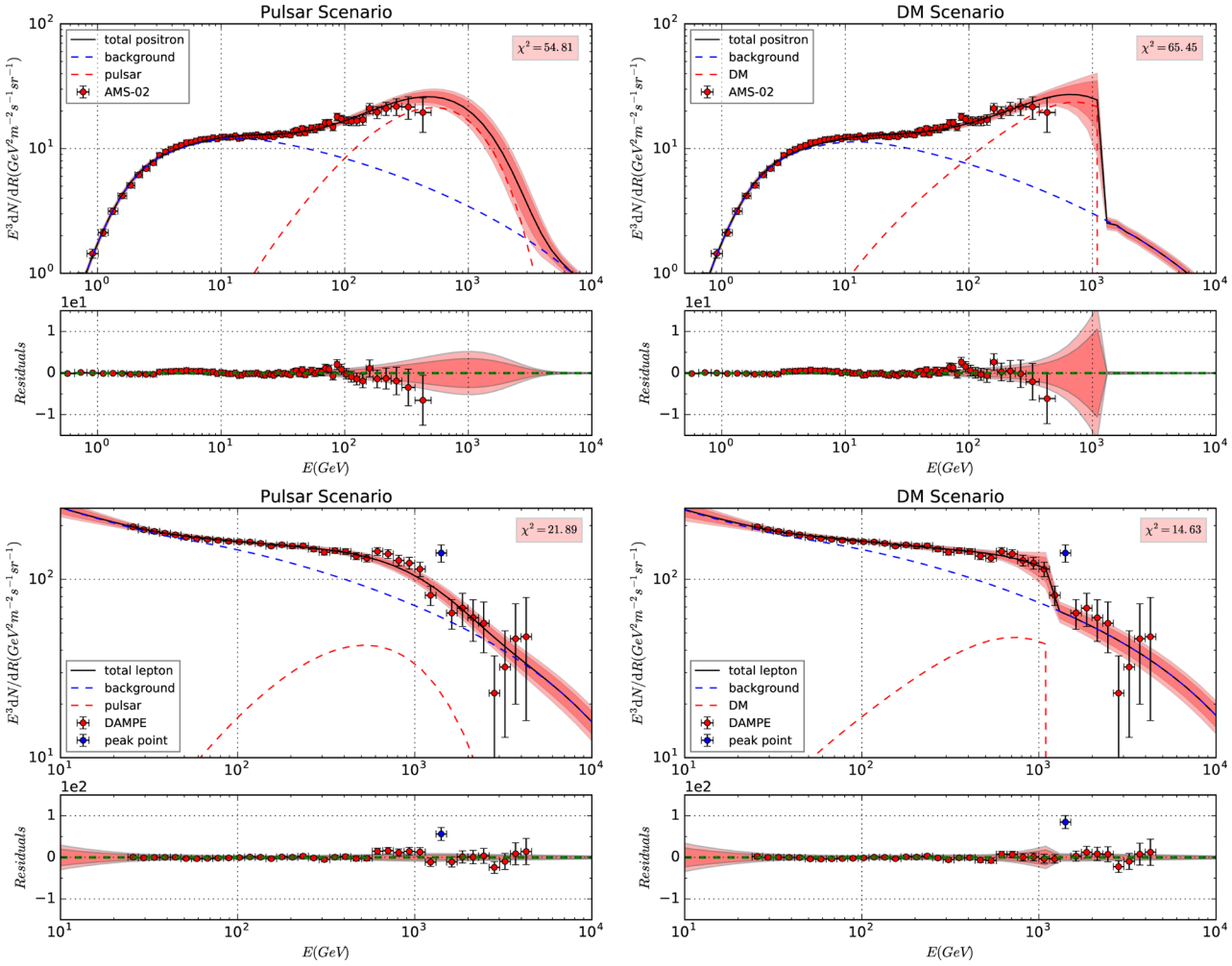

FIG. 2. Global fitting results and the corresponding residuals to the AMS-02 positron flux and *DAMPE* lepton flux. The 2σ (deep red) and 3σ (light red) bound are also shown. The first column shows the fitting results of pulsar and the second shows the fitting results of DM. For *DAMPE* CREs flux only, we got $\chi^2 = 21.89$ for the pulsar scenario and $\chi^2 = 14.63$ for the DM scenario.

The parameter sets for the pulsar scenario are

$$\begin{aligned}\boldsymbol{\theta}_{\rm psr} = \{&D_0, \delta, z_h, v_A, |N_{\rm p}, R_{\rm p1}, R_{\rm p2}, \nu_{\rm p1}, \nu_{\rm p2}, \nu_{\rm p3},\\ &R_{\rm He1}, R_{\rm He2}, \nu_{\rm He1}, \nu_{\rm He2}, \nu_{\rm He3}, |c_{\bar{\rm p}}, c_{\rm He}, \phi_{\rm nuc}, \phi_{\bar{\rm p}}, |\\ &N_{\rm e}, R_{\rm e1}, \nu_{\rm e1}, \nu_{\rm e2}, |\\ &N_{\rm psr}, \nu_{\rm psr}, R_c, |\\ &c_{e^+}, \phi_{e^+}\}\end{aligned}$$

and for the DM scenario are

$$\begin{aligned}\boldsymbol{\theta}_{\rm DM} = \{&D_0, \delta, z_h, v_A, |N_{\rm p}, R_{\rm p1}, R_{\rm p2}, \nu_{\rm p1}, \nu_{\rm p2}, \nu_{\rm p3},\\ &R_{\rm He1}, R_{\rm He2}, \nu_{\rm He1}, \nu_{\rm He2}, \nu_{\rm He3}, |c_{\bar{\rm p}}, c_{\rm He}, \phi_{\rm nuc}, \phi_{\bar{\rm p}}, |\\ &N_{\rm e}, R_{\rm e1}, \nu_{\rm e1}, \nu_{\rm e2}, |\\ &m_\chi, \langle\sigma v\rangle, \eta_e, \eta_\mu, \eta_\tau, |\\ &c_{e^+}, \phi_{e^+}\}.\end{aligned}$$

Note that, most of these two scenarios' parameters in the set $\boldsymbol{\theta}_{\rm psr}$ and $\boldsymbol{\theta}_{\rm DM}$ are the same as the other except for those that account for the extra sources of lepton.

IV. FITTING RESULTS AND DISCUSSION

The MCMC algorithm was used to determine the parameters in the two scenarios. When the Markov chains have reached their equilibrium state, we take the samples of the parameters as their posterior PDFs. The best-fitting results and the corresponding residuals of the proton flux, helium flux, and $\bar{\rm p}/{\rm p}$ ratio for the two scenarios are shown in Fig. 1, and the corresponding results of the positron and CRE flux are shown in Fig. 2. The best-fit values, statistical mean values, standard deviations, and allowed intervals at 95% C.L. for parameters in set $\boldsymbol{\theta}_{\rm psr}$ and $\boldsymbol{\theta}_{\rm DM}$ are shown in Table I and Table II, respectively. For best-fit results of the global fitting, we

TABLE I. Constraints on the parameters in set $\boldsymbol{\theta}_{\rm psr}$. The prior interval, best-fit value, statistic mean, standard deviation, and the allowed range at 95% C.L. are listed for parameters, with $\chi^2/\text{d.o.f} = 255.24/298$ for best-fit result.

ID	Prior range	Best-fit value	Posterior mean and standard deviation	Posterior 95% range
D_0 (10^{28} cm^2 s^{-1})	[1, 20]	14.37	14.38 ± 0.16	[13.95, 14.74]
δ	[0.1, 1.0]	0.318	0.317 ± 0.003	[0.311, 0.326]
z_h (kpc)	[0.5, 30.0]	25.08	25.13 ± 0.22	[24.55, 25.69]
v_A (km/s)	[0, 80]	41.34	41.34 ± 0.38	[40.37, 42.32]
N_p[a]	[1, 8]	4.46	4.46 ± 0.01	[4.44, 4.49]
$R_{\rm p1}$ (GV)	[1, 30]	25.88	25.78 ± 0.20	[25.43, 26.41]
$R_{\rm p2}$ (GV)	[60, 1000]	428.98	429.05 ± 7.44	[409.86, 447.63]
$\nu_{\rm p1}$	[1.0, 4.0]	2.196	2.198 ± 0.006	[2.180, 2.209]
$\nu_{\rm p2}$	[1.0, 4.0]	2.465	2.464 ± 0.005	[2.453, 2.474]
$\nu_{\rm p3}$	[1.0, 4.0]	2.348	2.349 ± 0.008	[2.332, 2.368]
$R_{\rm He1}$ (GV)	[1, 30]	12.07	12.09 ± 0.15	[11.67, 12.50]
$R_{\rm He2}$ (GV)	[60, 1000]	244.83	246.41 ± 8.14	[220.09, 265.47]
$\nu_{\rm He1}$	[1.0, 4.0]	2.186	2.188 ± 0.007	[2.170, 2.199]
$\nu_{\rm He2}$	[1.0, 4.0]	2.422	2.422 ± 0.005	[2.411, 2.431]
$\nu_{\rm He3}$	[1.0, 4.0]	2.219	2.219 ± 0.012	[2.197, 2.241]
$\phi_{\rm nuc}$ (GV)	[0, 1.5]	0.73	0.73 ± 0.01	[0.71, 0.76]
$\phi_{\bar{\rm p}}$ (GV)	[0, 1.5]	0.28	0.28 ± 0.01	[0.26, 0.30]
$c_{\rm He}$	[0.1, 10.0]	3.93	3.89 ± 0.11	[3.66, 4.22]
$c_{\bar{\rm p}}$	[0.1, 10.0]	1.37	1.37 ± 0.02	[1.34, 1.41]
$\log(N_{\rm e})$[b]	[−4, 0]	−1.936	-1.936 ± 0.006	[−1.950, −1.926]
$\log(R_{\rm e}/\text{GV})$	[0, 3]	1.64	1.64 ± 0.03	[1.55, 1.75]
$\nu_{\rm e1}$	[1.0, 4.0]	2.56	2.57 ± 0.02	[2.50, 2.61]
$\nu_{\rm e2}$	[1.0, 4.0]	2.39	2.39 ± 0.01	[2.36, 2.42]
$\log(N_{\rm psr})$[c]	[−8, −4]	−6.15	-6.15 ± 0.02	[−6.19, −6.11]
$\nu_{\rm psr}$	[0, 3.0]	0.65	0.65 ± 0.01	[0.61, 0.69]
$\log(R_c/\text{GV})$)	[2, 5]	2.81	2.80 ± 0.02	[2.78, 2.86]
ϕ_{e^+} (GV)	[0, 1.5]	1.37	1.37 ± 0.01	[1.36, 1.39]
c_{e^+}	[0.1, 10.0]	5.09	5.08 ± 0.05	[5.03, 5.15]

[a]Post-propagated normalization flux of protons at 100 GeV in unit 10^{-2} m^{-2} s^{-1} sr^{-1} GeV^{-1}.
[b]Post-propagated normalization flux of electrons at 25 GeV in unit m^{-2} s^{-1} sr^{-1} GeV^{-1}.
[c]Post-propagated normalization flux of electrons at 300 GeV in unit m^{-2} s^{-1} sr^{-1} GeV^{-1}.

got $\chi^2/\text{d.o.f} = 255.24/298$ for the pulsar scenario and $\chi^2/\text{d.o.f} = 276.56/296$ for the DM scenario.[3]

In Fig. 1, we can see that the nuclei data are perfectly reproduced, which would provide a good precondition for the subsequent fitting on the lepton data. The proton and helium particles $\gtrsim$TeV would produce the secondary particles (including antiprotons and positrons) in a lower energy range. Although the CREAM proton and helium data $\gtrsim$TeV have relatively large uncertainties, the spectral hardening at ∼300 GeV is accounted for, and then its influence on secondary products is included.

The best-fitting results and the corresponding residuals of the lepton and positron spectra are shown in Fig. 2. The corresponding best-fit values, statistical mean values, standard deviations, and allowed intervals at 95% C.L. for these parameters are shown in Tables I and II.

In Fig. 2, the lepton data can be fitted within fitting uncertainties. Although we obtained smaller reduced χ^2 from global fitting on pulsar scenarios, if we consider the *DAMPE* CRE flux alone, the best-fit results show $\chi^2 = 21.89$ for the pulsar scenario and $\chi^2 = 14.63$ for the DM scenario.

[3]Considering the correlations between different parameters, we could not get a reasonable reduced χ^2 for each part of the data set independently. As a result, we showed the χ^2 for each part of the data set in Figs. 1 and 2.

TABLE II. The same as Table I, but for the ones in set $\boldsymbol{\theta}_{\rm DM}$, with $\chi^2/{\rm d.o.f} = 276.56/296$ for best-fit result.

ID	Prior range	Best-fit value	Posterior mean and standard deviation	Posterior 95% range
D_0 (10^{28} cm^2 s^{-1})	[1, 20]	15.72	15.76 ± 0.14	[15.47, 15.96]
δ	[0.1, 1.0]	0.307	0.307 ± 0.004	[0.302, 0.313]
z_h (kpc)	[0.5, 30.0]	28.59	28.39 ± 0.22	[28.07, 28.78]
v_A (km/s)	[0, 80]	42.46	42.60 ± 0.48	[41.69, 43.32]
N_p[a]	[1, 8]	4.50	4.48 ± 0.02	[4.45, 4.51]
$R_{\rm p1}$ (GV)	[1, 30]	23.18	23.19 ± 0.20	[22.92, 23.60]
$R_{\rm p2}$ (GV)	[60, 1000]	497.28	492.08 ± 8.41	[480.08, 507.07]
$\nu_{\rm p1}$	[1.0, 4.0]	2.222	2.226 ± 0.009	[2.212, 2.239]
$\nu_{\rm p2}$	[1.0, 4.0]	2.477	2.477 ± 0.006	[2.468, 2.486]
$\nu_{\rm p3}$	[1.0, 4.0]	2.357	2.352 ± 0.009	[2.338, 2.368]
$R_{\rm He1}$ (GV)	[1, 30]	11.06	11.23 ± 0.17	[10.97, 11.57]
$R_{\rm He2}$ (GV)	[60, 1000]	237.29	232.95 ± 8.88	[219.91, 248.52]
$\nu_{\rm He1}$	[1.0, 4.0]	2.206	2.207 ± 0.008	[2.196, 2.221]
$\nu_{\rm He2}$	[1.0, 4.0]	2.435	2.435 ± 0.005	[2.426, 2.443]
$\nu_{\rm He3}$	[1.0, 4.0]	2.232	2.232 ± 0.013	[2.213, 2.257]
$\phi_{\rm nuc}$ (GV)	[0, 1.5]	0.77	0.78 ± 0.01	[0.76, 0.80]
$\phi_{\bar{\rm p}}$ (GV)	[0, 1.5]	0.25	0.26 ± 0.01	[0.24, 0.27]
$c_{\rm He}$	[0.1, 10.0]	3.68	3.56 ± 0.11	[3.38, 3.74]
$c_{\bar{\rm p}}$	[0.1, 10.0]	1.47	1.47 ± 0.02	[1.44, 1.50]
$\log(N_{\rm e})$[b]	[−4, 0]	−1.940	-1.943 ± 0.007	[−1.958, −1.928]
$\log(R_{\rm e}/{\rm GV})$	[0, 3]	1.62	1.63 ± 0.04	[1.57, 1.74]
$\nu_{\rm e1}$	[1.0, 4.0]	2.55	2.54 ± 0.03	[2.46, 2.60]
$\nu_{\rm e2}$	[1.0, 4.0]	2.37	2.37 ± 0.01	[2.34, 2.40]
$\log(m_\chi/{\rm GeV})$	[1, 6]	3.082	3.085 ± 0.006	[3.076, 3.096]
$\log(\langle\sigma v\rangle)$[c]	[−28, −18]	−22.83	-22.80 ± 0.06	[−22.93, −22.70]
η_e	[0, 1]	0.484	0.479 ± 0.007	[0.466, 0.488]
η_μ	[0, 1]	0.508	0.508 ± 0.008	[0.493, 0.518]
η_τ	[0, 1]	0.008	0.013 ± 0.010	[0.001, 0.032]
ϕ_{e^+} (GV)	[0, 1.5]	1.32	1.31 ± 0.01	[1.296, 1.332]
c_{e^+}	[0.1, 10.0]	5.02	5.03 ± 0.03	[4.97, 5.08]

[a]Post-propagated normalization flux of protons at 100 GeV in unit 10^{-2} m^{-2} s^{-1} sr^{-1} GeV^{-1}.
[b]Post-propagated normalization flux of electrons at 25 GeV in unit m^{-2} s^{-1} sr^{-1} GeV^{-1}.
[c]In unit cm^3 s^{-1}.

A. Propagation parameters

The results of posterior probability distributions of the propagation parameters are shown in Fig. 3 (for the pulsar scenario) and Fig. 4 (for the DM scenario).

In this work, we adapt the widely used diffusion-reacceleration model to describe the propagation process, and the relevant propagation parameters are D_0, δ, z_h, and v_A. The obtained posterior PDFs are different from previous works to some extent. The classical degeneracy between D_0 and z_h is not obvious due to the data set in this work, but both of them get larger best-fit values than previous works. This is because (i) the D_0 defined in DRAGON (which represents the perpendicular diffusion coefficient $D_\perp$) is not the same as that in GALPROP (which represents the isotropic diffusion coefficient); (ii) the sensitivity region which could break the degeneracy between D_0 and z_h is different between $\bar{\rm p}/{\rm p}$ (10–100 GeV) and B/C ($\lesssim$10 GeV). The observed AMS-02 $\bar{\rm p}/{\rm p}$ ratio favors larger D_0 and z_h values.

The δ value obtained in this work is smaller than some of the previous works because we use one more break in the primary source injection of proton (∼240 GV) and helium (∼420–500 GV) to account for the observed hardening in their observed spectra, other than using only one break and letting δ compromise the different slopes in high-energy regions ($\gtrsim$240–500 GV) (see, e.g., Niu and Li

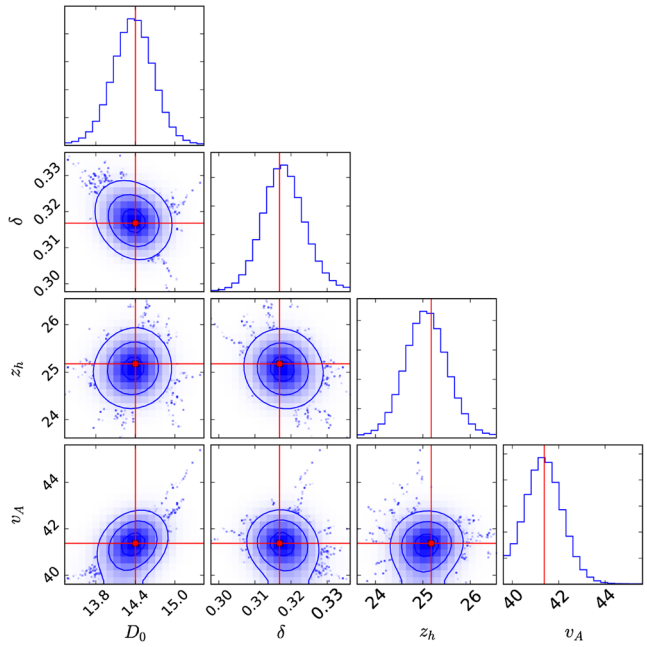

FIG. 3. Fitting 1D probability and 2D credible regions of posterior PDFs for the combinations of all propagation parameters for the pulsar scenario. The regions enclosing σ, 2σ, and 3σ C.L. are shown in step by step in lighter blue. The red cross lines and marks in each plot indicate the best-fit value (largest likelihood).

[49]). In such a configuration, we also got smaller fitting uncertainties on δ ($\sim$0.03).

Moreover, the fitting results favor relative large values of v_A, which may come from not only the constraints of nuclei data in low energy regions but also the positron data as well.

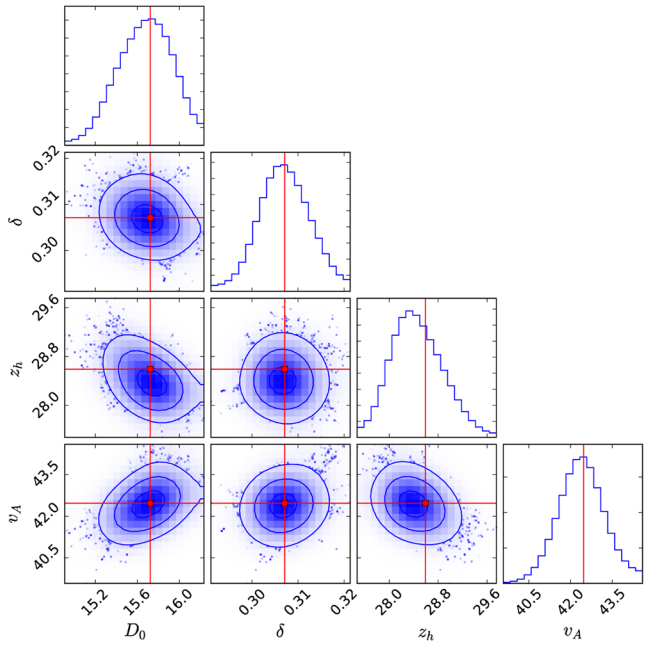

FIG. 4. Same as Fig. 3 but for the DM scenario.

B. Primary source injection parameters

The results of posterior probability distributions of the primary source parameters are shown in Figs. 5 (proton and helium, for the pulsar scenario), 6 (proton and helium, for the DM scenario), 7 (electron, for the pulsar scenario), and 8 (electron, for the DM scenario).

Benefitting from the two independent break injection spectra for proton and helium, the observed data have been reproduced perfectly. The fitting result shows that the rigidity breaks and the slopes are obviously different between proton and helium spectra. This indicates that cosmic-ray physics has entered a precision-driven era and that all these differences should be treated carefully in future studies. On the other hand, we want to point out that the hardening of the nuclei spectra at $\sim$300 GeV could also be reproduced by other proposals, which focus on the propagation and diffusion effects rather than ascribing it to the acceleration near the source. These solutions include proposing a spatial dependent diffusion coefficient [81–83] or adding a high-rigidity break in the diffusion coefficient [84–86]. With the precise data obtained in future extending to higher energy regions, we would expect more details to be revealed on this theme.

Additionally, the electron primary source injection spectra can be described by a break power-law from 20 GeV to 10^4 GeV (*DAMPE* data), with $\nu_{e1} \in [2.54, 2.57]$, $\nu_{e2} \in [2.37, 2.39]$, and $R_e \in [38, 47]$ GV.

C. Extra source parameters

The results for posterior probability distributions of the extra source parameters are shown in Figs. 9 (for the pulsar scenario) and 10 (for the DM scenario).

For the pulsar scenario, the fitting results give $\nu_{psr} \simeq 0.65$, which are obviously different from the fitting results in previous works (see, e.g., [14]). In standard pulsar models, the injection spectrum indices of CREs from pulsars are always in the range $\nu_{psr} \in [1.0, 2.4]$ [87–89]. As a result, more attention should be paid to this in future research. This may indicate that (i) there is something wrong or inaccurate with the classical pulsar CRE injection model and that (ii) the CRE excess is not contributed to dominatly by pulsars. Moreover, the rigidity cutoff is $R_c \simeq 646$ GV.

For the DM scenario, we obtain $\langle \sigma v \rangle \simeq 1.48 \times 10^{-23}\,\mathrm{cm^2\,s^{-1}}$ and $m_\chi \simeq 1208$ GeV. The value of $\langle \sigma v \rangle$ is about 3 orders larger than that of thermal DM [90]. Moreover, we have $\eta_e \simeq 0.484$, $\eta_\mu \simeq 0.508$, and $\eta_\tau \simeq 0.008$, which is obviously different from the fitting results obtained from AMS-02 lepton data alone (see, e.g., Lin *et al.* [47]). Consequently, the DM annihilation into $\tau\bar{\tau}$ is highly suppressed, which provides some hints to construct an appropriate DM model (see, e.g., [91]).

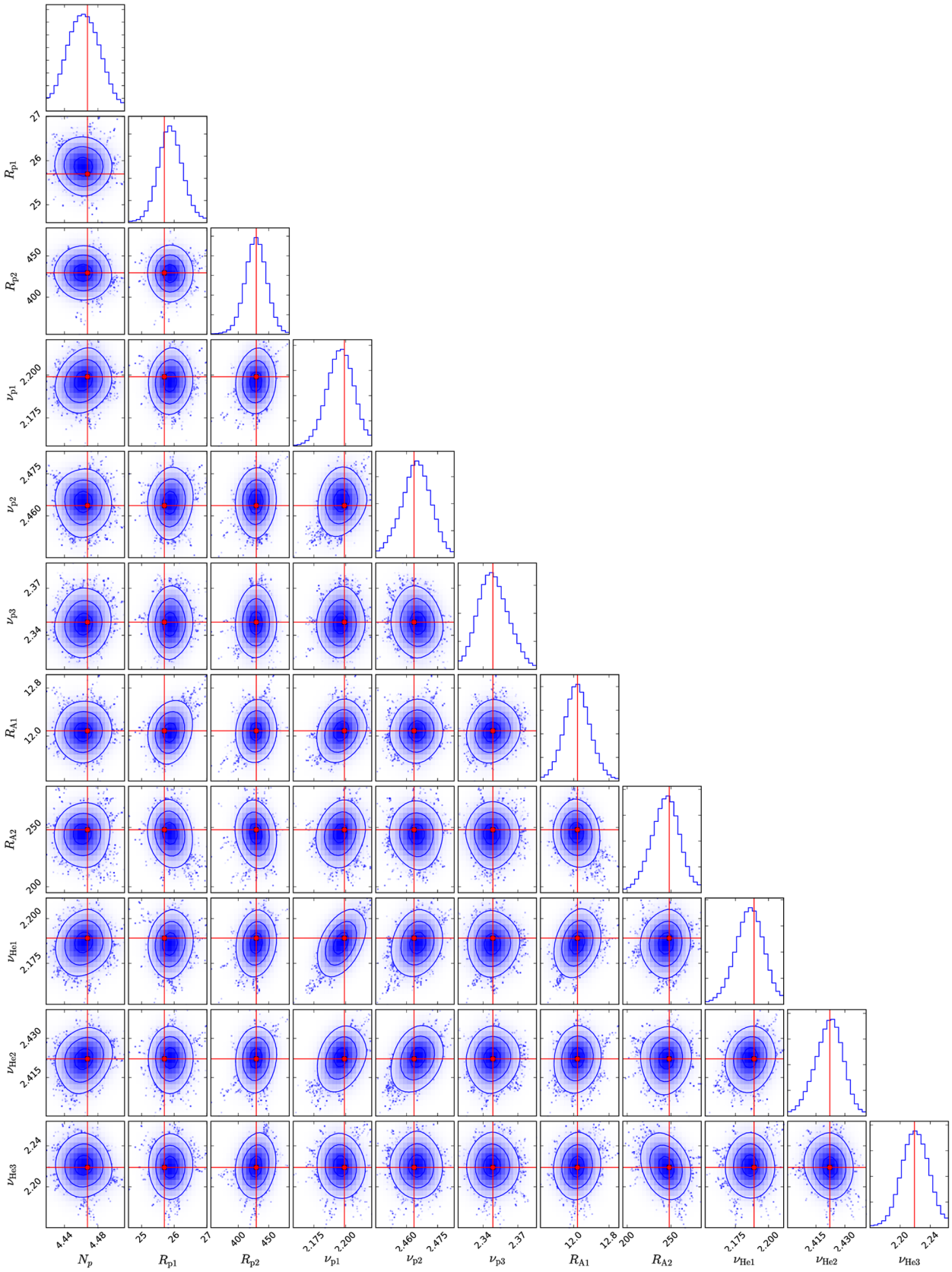

FIG. 5. Fitting 1D probability and 2D credible regions of posterior PDFs for the combinations of nuclei primary source injection parameters for the pulsar scenario. The regions enclosing σ, 2σ, and 3σ C.L. are shown in step by step in lighter blue. The red cross lines and marks in each plot indicate the best-fit value (largest likelihood).

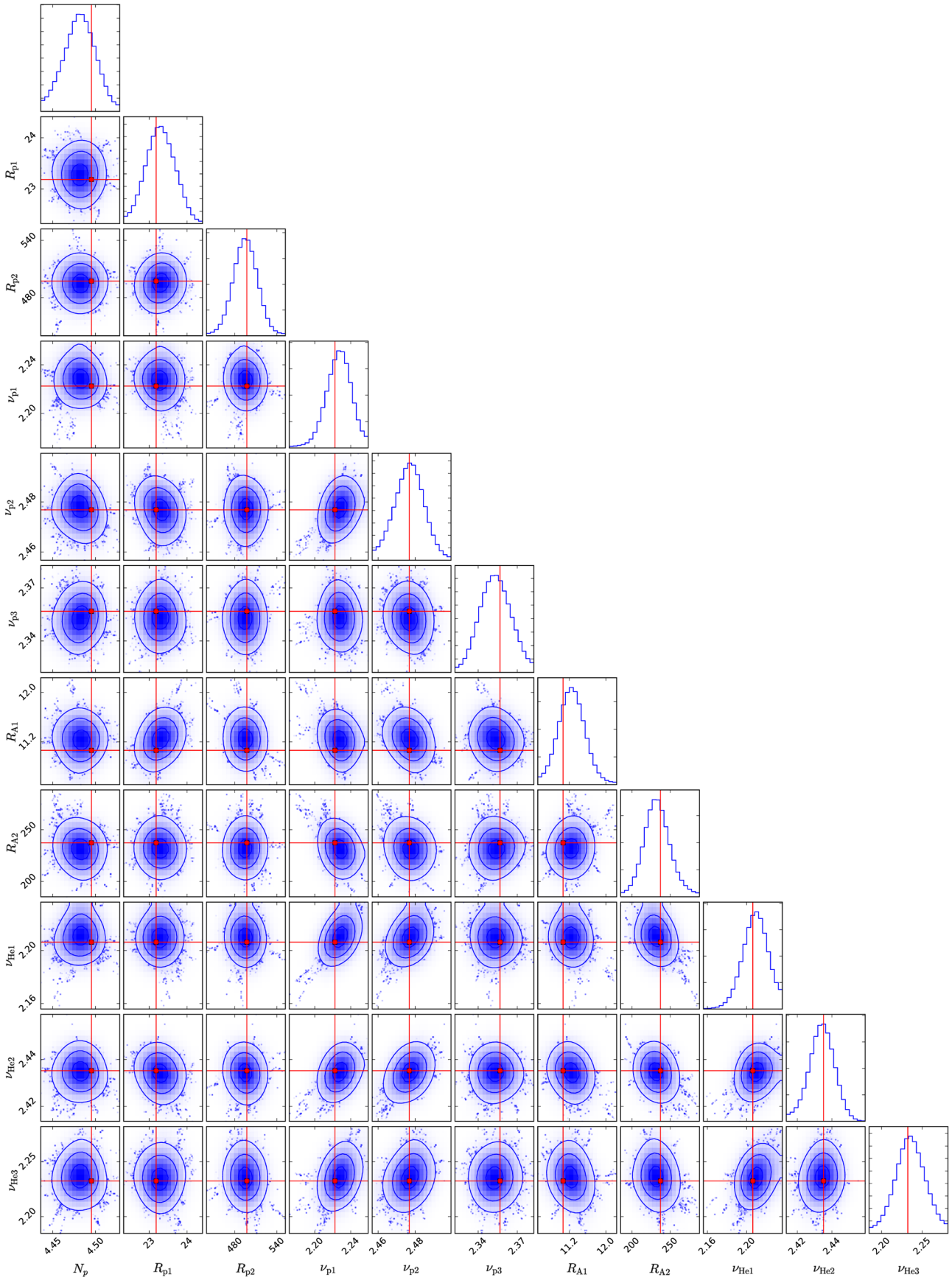

FIG. 6. Same as Fig. 5 but for the DM scenario.

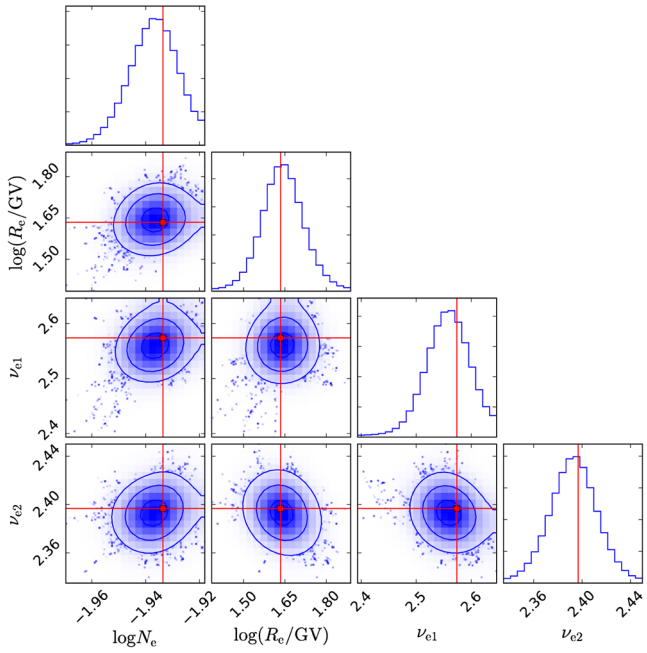

FIG. 7. Fitting 1D probability and 2D credible regions of posterior PDFs for the combinations of electron primary source injection parameters for the pulsar scenario. The regions enclosing σ, 2σ, and 3σ C.L. are shown in step by step in lighter blue. The red cross lines and marks in each plot indicate the best-fit value (largest likelihood).

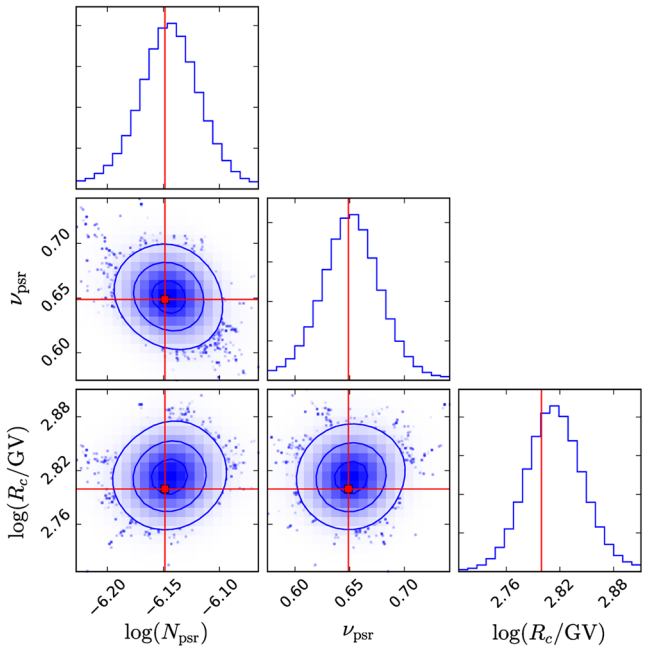

FIG. 9. Fitting 1D probability and 2D credible regions of posterior PDFs for the combinations of extra lepton soruce parameters for the pulsar scenario. The regions enclosing σ, 2σ, and 3σ C.L. are shown in step by step in lighter blue. The red cross lines and marks in each plot indicate the best-fit value (largest likelihood).

Because we have $\eta_e \simeq 0.484$, $\eta_\mu \simeq 0.508$, and $\eta_\tau \simeq 0.008$, the constraints from the Fermi-LAT observations on dwarf spheroidal galaxies [24,92–96] can be avoided [17]. In order to escape the constraints from the Planck observations of cosmic microwave background anisotropies [97], the Breit-Wigner mechanism [98–105] could be employed, and the dark $U(1)_D$ model (where the SM fermions and Higgs fields are neutral under it) could be considered.

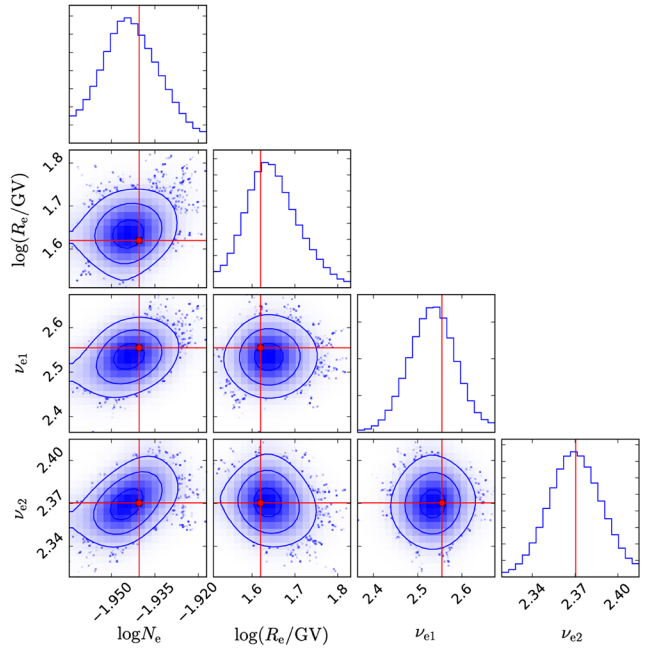

FIG. 8. Same as Fig. 7 but for the DM scenario.

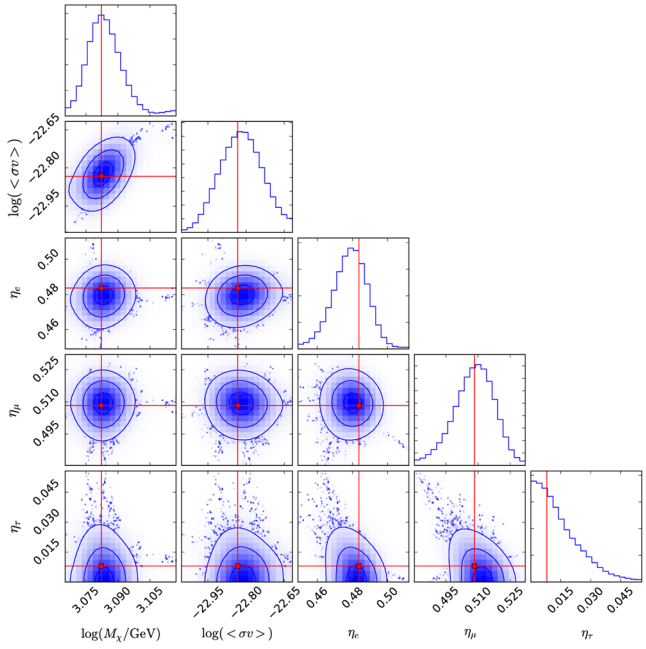

FIG. 10. Same as Fig. 9 but for the DM scenario.

We introduce one SM singlet field S, one chiral fermionic dark matter particle χ, and three pairs of the vectorlike particles ($\widehat{XE}_i$, $\widehat{XE}_i^c$), whose quantum numbers under the $SU(3)_C \times SU(2)_L \times U(1)_Y \times U(1)_D$ are

$$\begin{aligned} S&: (\mathbf{1},\mathbf{1},\mathbf{0},\mathbf{2}), \qquad \chi: (\mathbf{1},\mathbf{1},\mathbf{0},\mathbf{-1}) \\ \widehat{XE}_i&: (\mathbf{1},\mathbf{1},\mathbf{-1},\mathbf{-2}), \qquad \widehat{XE}_i^c: (\mathbf{1},\mathbf{1},\mathbf{1},\mathbf{2}). \end{aligned} \tag{6}$$

The relevant Lagrangian is

$$\begin{aligned} -\mathcal{L} = &-m_S^2|S|^2 + \frac{\lambda}{2}|S|^4 + (M_{ij}^V \widehat{XE}_i^c \widehat{XE}_j \\ &+ y_{ij} S \hat{E}_i^c \widehat{XE}_j + y S \chi\chi + \text{H.c.}), \end{aligned} \tag{7}$$

where $\hat{E}_i^c$ are the right-handed charged leptons.

For simplicity, we choose $M_{ij}^V = M_i^V \delta_{ij}$ and $y_{ij} = y_i \delta_{ij}$. After S acquires a vacuum expectation value (VEV), the $U(1)_D$ gauge symmetry is broken down to a Z_2 symmetry under which χ is odd. Thus, χ is a DM matter candidate. For simplicity, we assume that the mass of the $U(1)_D$ gauge boson is about twice that of χ mass, *i.e.*, $M_{Z'} \simeq 2m_\chi$, while the Higgs field S and vectorlike particles are heavier than $M_{Z'}$. Moreover, $\hat{E}_i^c$ and $\widehat{XE}_i^c$ will be mixed due to the $M_i^V \widehat{XE}_i^c \widehat{XE}_i$ and $y_i S \hat{E}_i^c \widehat{XE}_i$ terms, and we obtain the mass eigenstates E_i^c and XE_i^c by neglecting the tiny charged lepton masses

$$\begin{pmatrix} E_i^c \\ XE_i^c \end{pmatrix} = \begin{pmatrix} \cos\theta_i & \sin\theta_i \\ -\sin\theta_i & \cos\theta_i \end{pmatrix} \begin{pmatrix} \hat{E}_i^c \\ \widehat{XE}_i^{c\prime} \end{pmatrix}, \tag{8}$$

where $\tan\theta_i = -y\langle S\rangle / M_i^V$.

Neglecting the charged lepton masses again, we obtain

$$\sigma v = \sum_{i=1}^{3} \frac{g'^4 \sin^2\theta_i}{6\pi} \frac{s - m_\chi^2}{(s - m_{Z'}^2)^2 + (m_{Z'}\Gamma_{Z'})^2}, \tag{9}$$

where $m_\chi = y\langle S\rangle$, and g' and $M_{Z'}$ are the gauge coupling and gauge boson mass for $U(1)_D$ gauge symmetry, respectively.

For $m_{Z'} \simeq 2m_\chi$, Z' decays dominantly into leptons, and the decay width is

$$\Gamma_{Z'} = \sum_{i=1}^{3} \frac{g'^2 \sin^2\theta_i}{6\pi} m_{Z'}. \tag{10}$$

To explain the DM best-fit results, we can choose proper values of g', $\frac{m_{Z'} - 2m_\chi}{m_{Z'}}$, $\sin\theta_e$, $\sin\theta_\mu$, and $\sin\theta_\tau$ to reproduce the values of m_χ, $\langle\sigma v\rangle$ and $\eta_e : \eta_\mu : \eta_\tau$ like that in Niu *et al.* [106].

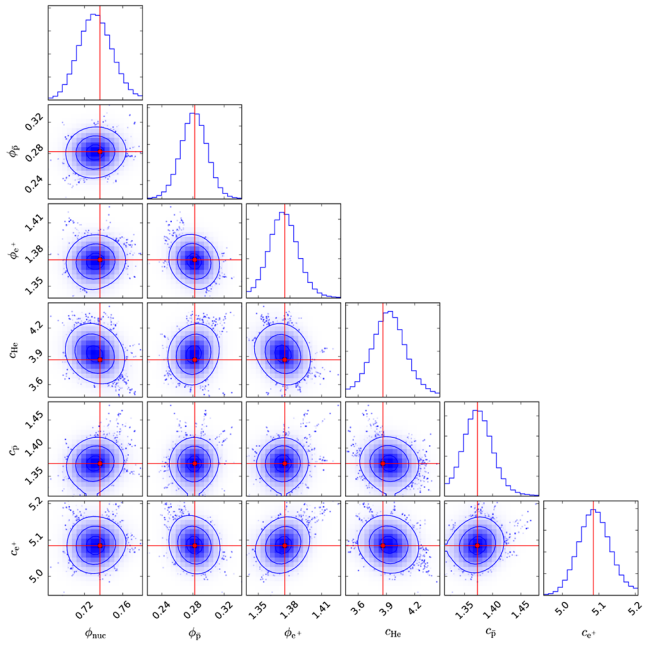

FIG. 11. Fitting 1D probability and 2D credible regions of posterior PDFs for the combinations of nuisance parameters for the pulsar scenario. The regions enclosing σ, 2σ, and 3σ C.L. are shown step by step in lighter blue. The red cross lines and marks in each plot indicate the best-fit value (largest likelihood).

D. Nuisance parameters

In Figs 11 and 12, the results of posterior probability distributions represent the necessity to introduce them in the global fitting.

The different values of ϕ_{nuc}, $\phi_{\bar{\text{p}}}$, and ϕ_{e^+} from the best-fit results represent not only the charge-sign-dependent solar

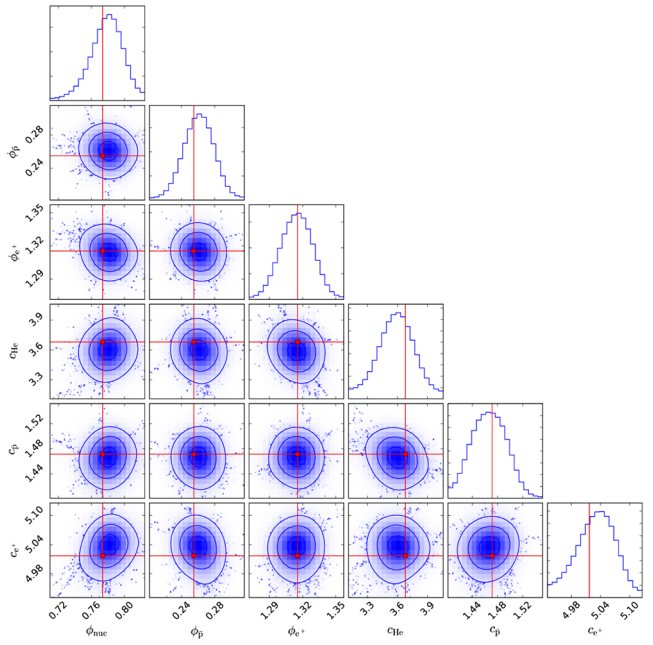

FIG. 12. Same as Fig. 11 but for the DM scenario.

modulation (which has also been claimed by some previous works, see, e.g., Niu and Li [107], Clem *et al.* [108], and Boella *et al.* [49]) but also a species dependent solar modulation to some extent. As claimed in our previous works [49], the force field approximation could not describe the effects of solar modulation to all the species by a single ϕ, but as an effective model, we can use an independent ϕ for each of the species.[4] The different values of the ϕs for different species could reveal the hints to improve their propagation mechanisms in the heliosphere. Additionally, the proton, helium, and positron data have been collected from AMS-02 in the same period with a suggested ϕ from 0.50 to 0.62 GV [30,53,54], which is based on data from the world network of sea level neutron monitors [109]. More details in this field can be obtained in Corti *et al.* [110].

The value of $c_{\bar{\mathrm{p}}} \sim 1.4$–$1.5$ could be explained by the uncertainties on the antiproton production cross section [58–61,111].

The DRAGON primary source isotopic abundances are inherited from GALPROP, which are taken as the solar system abundances and iterated to achieve an agreement with the propagated abundances as provided by ACE at ~200 MeV nucleon. It is natural that the normalized factor is different in different energy regions. On the other hand, we always focus on the shape of the spectrum, and c_{He} could be considered as an independent normalized factor as N_p, which is identified as a nuisance parameter to get a better fitting result and is not that important in this work.

For c_{e^+}, there are several reasons which could be ascribed to its relatively large values: (i) the cross section comes from Kamae *et al.* [112,113], which needed a scale factor to correlate its values [114]; (ii) the systematics between the *DAMPE* CRE spectrum and AMS-02 positron spectrum is also partially accounted for in the parameter c_{e^+}, which leads to c_{e^+} that is not just an indicator of rescale factor on cross section. Moreover, we would like to point out that in this work, we focus on the extra sources which would reproduce the break at ~1 TeV in *DAMPE* CRE data. Some nuisance parameters ($c_{\bar{\mathrm{p}}}$, c_{He}, and c_{e^+}) are employed to fit all the data consistently and precisely (especially the primary source and background; see, e.g., Lin *et al.* [47]), which may not have clear physical meanings but could also give us some hints to improve the details in CR physics in future research.

V. CONCLUSION

In this work, we did Bayesian analysis on the newly released CRE flux (excluding the peak signal at ~1.4 TeV) from *DAMPE* to study the extra source properties in it. In order to deduct the primary electrons and secondary leptons in CRE flux consistently and precisely, we did a global fitting to reproduce the proton flux (from AMS-02 and CREAM), helium flux (from AMS-02 and CREAM), $\bar{\mathrm{p}}/\mathrm{p}$ ratio (from AMS-02), positron flux (from AMS-02), and CRE flux (from *DAMPE*) simultaneously. Two independent extra source scenarios are considered, which account for the excess of leptons to be continuously distributed pulsars in the galaxy and dark matter annihilation (via leptonic channels) in the galactic halo. Both of these scenarios can fit the *DAMPE* CRE flux within the fitting uncertainties, while the DM scenario gave a smaller χ^2 and an obvious break at ~1 TeV.

Additionally, in the DM scenario, the fitting result gives a dark matter particle's mass $m_\chi \sim 1208$ GeV and a cross section $\langle\sigma v\rangle \sim 1.48 \times 10^{-23}$ cm^3 s^{-1}. This benefited from the break at ~1 TeV. In such situations, the cross section in this work still should have a suppression factor to meet the value $\langle\sigma v\rangle \sim 3 \times 10^{-26}$ cm^3 s^{-1}. This discrepancy can be resolved by some proposed mechanisms like the nonthermal production of the DM [115–117], the Sommerfeld enhancement mechanism [118–120], and Breit-Wigner type resonance of the annihilation interaction [121,122]. What is more interesting, the constraints on the annihilation branching fraction shows that the $\tau\bar{\tau}$ annihilation channel is strongly suppressed, while the e^-e^+ and $\mu\bar{\mu}$ channels are almost equally weighted ($\eta_e = 0.484$, $\eta_\mu = 0.508$, and $\eta_\tau = 0.008$). This would give some hints for constructing DM models, and we tried to build one in this work to meet the fitting results.

Note, in this work we can see that the CRE spectrum from *DAMPE* without the peak can be reproduced by DM scenarios precisely. On the other hand, the spectrum with the peak also can be reproduced by DM annihilation from a local DM substructure [17–23,123–126]. Both of these situations call for DM particles with $m_\chi \sim 1$–2 TeV. Another independent detection strategy is needed to distinguish the excess in the CRE spectrum, which can also be produced from some astrophysical sources [16,17,127]. Our recent works [128] proposed a novel scenario to probe the interaction between DM particles and electrons with 5 GeV $\lesssim m_\chi \lesssim$ 10 TeV.

ACKNOWLEDGMENTS

We would like to thank Maurin *et al.* [129] for collecting database and associated online tools for charged cosmic-ray measurements, and Foreman-Mackey *et al.* [130] for providing us the tool to visualize multidimensional samples using a scatterplot matrix. Many thanks to the referees for valuable and detailed suggestions, which led to great progress in this work. This research was supported in part by Projects No. 11475238 and No. 11647601 supported by National Science Foundation of China, and by Key Research Program of Frontier Sciences, CAS. The calculations in this paper are supported by HPC Cluster of SKLTP/ITP-CAS.

[4]In this work, we use a single ϕ_{nuc} to modulate the spectra of proton and helium simultaneously because a single ϕ_{nuc} could reproduce the low energy proton and helium spectra precisely under the precision of current data.

[1] J. Chang, Dark matter particle explorer: The first chinese cosmic ray and hard gamma-ray detector in space, Chinese Journal of Space Science / Kongjian Kexue Xuebao **34**, 550 (2014).

[2] J. Chang *et al.* (DAMPE), The DArk Matter Particle Explorer mission, Astropart. Phys. **95**, 6 (2017).

[3] G. Ambrosi *et al.* (DAMPE), Direct detection of a break in the teraelectronvolt cosmic-ray spectrum of electrons and positrons, Nature (London) **552**, 63 (2017).

[4] O. Adriani, G. C. Barbarino, G. A. Bazilevskaya, R. Bellotti, M. Boezio, E. A. Bogomolov, L. Bonechi, M. Bongi, V. Bonvicini, S. Bottai *et al.*, An anomalous positron abundance in cosmic rays with energies 1.5–100 GeV, Nature (London) **458**, 607 (2009).

[5] O. Adriani *et al.* (PAMELA Collaboration), A statistical procedure for the identification of positrons in the PAMELA experiment, Astropart. Phys. **34**, 1 (2010).

[6] M. Aguilar *et al.* (AMS Collaboration), Precision Measurement of the $(e^+ + e^-)$ Flux in Primary Cosmic Rays from 0.5 GeV to 1 TeV with the Alpha Magnetic Spectrometer on the International Space Station, Phys. Rev. Lett. **113**, 221102 (2014).

[7] M. Ackermann *et al.* (Fermi-LAT Collaboration), Measurement of Separate Cosmic-Ray Electron and Positron Spectra with the Fermi Large Area Telescope, Phys. Rev. Lett. **108**, 011103 (2012).

[8] O. Adriani *et al.* (CALET Collaboration), Energy Spectrum of Cosmic-Ray Electron and Positron from 10 GeV to 3 TeV Observed with the Calorimetric Electron Telescope on the International Space Station, Phys. Rev. Lett. **119**, 181101 (2017).

[9] S. Abdollahi *et al.* (Fermi-LAT Collaboration), Cosmic-ray electron-positron spectrum from 7 GeV to 2 TeV with the Fermi large area telescope, Phys. Rev. D **95**, 082007 (2017).

[10] D. Malyshev, I. Cholis, and J. Gelfand, Pulsars versus dark matter interpretation of ATIC/PAMELA, Phys. Rev. D **80**, 063005 (2009).

[11] M. Kuhlen and D. Malyshev, ATIC, PAMELA, HESS, and Fermi data and nearby dark matter subhalos, Phys. Rev. D **79**, 123517 (2009).

[12] P. Brun, T. Delahaye, J. Diemand, S. Profumo, and P. Salati, Cosmic ray lepton puzzle in the light of cosmological N-body simulations, Phys. Rev. D **80**, 035023 (2009).

[13] L. Gendelev, S. Profumo, and M. Dormody, The contribution of Fermi gamma-ray pulsars to the local flux of cosmic-ray electrons and positrons, J. Cosmol. Astropart. Phys. 2 (2010) 016.

[14] S. Profumo, Dissecting cosmic-ray electron-positron data with Occam's razor: the role of known pulsars, Central Eur. J. Phys. **10**, 1 (2012).

[15] A. D. Panov, Electrons and Positrons in Cosmic Rays, J. Phys. Conf. Ser. **409**, 012004 (2013).

[16] K. Fang, X.-J. Bi, and P.-F. Yin, Explanation of the knee-like feature in the DAMPE cosmic $e^- + e^+$ energy spectrum, Astrophys. J. **854**, 57 (2018).

[17] Q. Yuan *et al.*, Interpretations of the DAMPE electron data, arXiv:1711.10989.

[18] P. Athron, C. Balazs, A. Fowlie, and Y. Zhang, Model-independent analysis of the DAMPE excess, J. High Energy Phys. 02 (2018) 121.

[19] Y.-Z. Fan, W.-C. Huang, M. Spinrath, Y.-L. Sming Tsai, and Q. Yuan, A model explaining neutrino masses and the DAMPE cosmic ray electron excess, arXiv:1711.10995.

[20] G. H. Duan, L. Feng, F. Wang, L. Wu, J. M. Yang, and R. Zheng, Simplified TeV leptophilic dark matter in light of DAMPE data, J. High Energy Phys. 02 (2018) 107.

[21] P.-H. Gu and X.-G. He, Electrophilic dark matter with dark photon: from DAMPE to direct detection, Phys. Lett. B **778**, 292 (2018).

[22] X. Liu and Z. Liu, TeV dark matter and the DAMPE electron excess, arXiv:1711.11579.

[23] J. Cao, L. Feng, X. Guo, L. Shang, F. Wang, and P. Wu, Scalar dark matter interpretation of the DAMPE data with U(1) gauge interactions, arXiv:1711.11452.

[24] S. Profumo, F. S. Queiroz, J. Silk, and C. Siqueira, Searching for Secluded Dark Matter with H.E.S.S., Fermi-LAT, and Planck, J. Cosmol. Astropart. Phys. 03 (2018) 010.

[25] M. Aguilar *et al.* (AMS Collaboration), First Result from the Alpha Magnetic Spectrometer on the International Space Station: Precision Measurement of the Positron Fraction in Primary Cosmic Rays of 0.5–350 GeV, Phys. Rev. Lett. **110**, 141102 (2013).

[26] S. W. Barwick *et al.* (HEAT Collaboration), Measurements of the cosmic-ray positron fraction from 1 to 50 GeV, Astrophys. J. Lett. **482**, L191 (1997).

[27] AMS-01 Collaboration, Cosmic-ray positron fraction measurement from 1 to 30 GeV with AMS-01, Phys. Lett. B **646**, 145 (2007).

[28] M. Aguilar *et al.* (AMS Collaboration), First Result from the Alpha Magnetic Spectrometer on the International Space Station: Precision Measurement of the Positron Fraction in Primary Cosmic Rays of 0.5–350 GeV, Phys. Rev. Lett. **110**, 141102 (2013).

[29] L. Accardo *et al.* (AMS Collaboration), High Statistics Measurement of the Positron Fraction in Primary Cosmic Rays of 0.5–500 GeV with the Alpha Magnetic Spectrometer on the International Space Station, Phys. Rev. Lett. **113**, 121101 (2014).

[30] M. Aguilar *et al.* (AMS Collaboration), Electron and Positron Fluxes in Primary Cosmic Rays Measured with the Alpha Magnetic Spectrometer on the International Space Station, Phys. Rev. Lett. **113**, 121102 (2014).

[31] C. S. Shen, Pulsars and very high-energy cosmic-ray electrons, Astrophys. J. Lett. **162**, L181 (1970).

[32] L. Zhang and K. S. Cheng, Cosmic-ray positrons from mature gamma-ray pulsars, Astron. Astrophys. **368**, 1063 (2001).

[33] H. Yüksel, M. D. Kistler, and T. Stanev, TeV Gamma Rays from Geminga and the Origin of the GeV Positron Excess, Phys. Rev. Lett. **103**, 051101 (2009).

[34] D. Hooper, P. Blasi, and P. Dario Serpico, Pulsars as the sources of high energy cosmic ray positrons, J. Cosmol. Astropart. Phys. 1 (2009) 025.

[35] P. Blasi, Origin of the Positron Excess in Cosmic Rays, Phys. Rev. Lett. **103**, 051104 (2009).

[36] H.-B. Hu, Q. Yuan, B. Wang, C. Fan, J.-L. Zhang, and X.-J. Bi, On the e^+e^- excesses and the knee of the cosmic ray spectra hints of cosmic ray acceleration in young supernova remnants, Astrophys. J. Lett. **700**, L170 (2009).
[37] Y. Fujita, K. Kohri, R. Yamazaki, and K. Ioka, Is the PAMELA anomaly caused by supernova explosions near the Earth?, Phys. Rev. D **80**, 063003 (2009).
[38] L. Bergström, T. Bringmann, and J. Edsjö, New positron spectral features from supersymmetric dark matter: A way to explain the PAMELA data?, Phys. Rev. D **78**, 103520 (2008).
[39] V. Barger, W.-Y. Keung, D. Marfatia, and G. Shaughnessy, PAMELA and dark matter, Phys. Lett. B **672**, 141 (2009).
[40] M. Cirelli, M. Kadastik, M. Raidal, and A. Strumia, Model-independent implications of the e^+, e^-, anti-proton cosmic ray spectra on properties of Dark Matter, Nucl. Phys. **B813**, 1 (2009).
[41] J. Zhang, X.-J. Bi, J. Liu, S.-M. Liu, P.-F. Yin, Q. Yuan, and S.-H. Zhu, Discriminating different scenarios to account for the cosmic e^+ excess by synchrotron and inverse Compton radiation, Phys. Rev. D **80**, 023007 (2009).
[42] L. Bergström, J. Edsjö, and G. Zaharijas, Dark Matter Interpretation of Recent Electron and Positron Data, Phys. Rev. Lett. **103**, 031103 (2009).
[43] P.-F. Yin, Z.-H. Yu, Q. Yuan, and X.-J. Bi, Pulsar interpretation for the AMS-02 result, Phys. Rev. D **88**, 023001 (2013).
[44] P. S. B. Dev, D. K. Ghosh, N. Okada, and I. Saha, Neutrino mass and dark matter in light of recent AMS-02 results, Phys. Rev. D **89**, 095001 (2014).
[45] A. Lewis and S. Bridle, Cosmological parameters from CMB and other data: A Monte Carlo approach, Phys. Rev. D **66**, 103511 (2002).
[46] J. Liu, Q. Yuan, X. Bi, H. Li, and X. Zhang, Markov chain Monte Carlo study on dark matter property related to the cosmic e^+ excesses, Phys. Rev. D **81**, 023516 (2010).
[47] S.-J. Lin, Q. Yuan, and X.-J. Bi, Quantitative study of the ams-02 electron/positron spectra: implications for the pulsar and dark matter properties, Phys. Rev. D **91**, 063508 (2015).
[48] Q. Yuan, S.-J. Lin, K. Fang, and X.-J. Bi, Propagation of cosmic rays in the AMS-02 era, Phys. Rev. D **95**, 083007 (2017).
[49] J.-S. Niu and T. Li, Galactic cosmic-ray model in the light of AMS-02 nuclei data, Phys. Rev. D **97**, 023015 (2018).
[50] A. D. Panov *et al.*, The results of ATIC-2 experiment for elemental spectra of cosmic rays, Bull. Russ. Acad. Sci. Phys. **71**, 494 (2007).
[51] H. S. Ahn *et al.*, Discrepant hardening observed in cosmic-ray elemental spectra, Astrophys. J. Lett. **714**, L89 (2010).
[52] O. Adriani *et al.* (PAMELA Collaboration), PAMELA measurements of cosmic-ray proton and helium spectra, Science **332**, 69 (2011).
[53] M. Aguilar *et al.* (AMS Collaboration), Precision Measurement of the Proton Flux in Primary Cosmic Rays from Rigidity 1 GV to 1.8 TV with the Alpha Magnetic Spectrometer on the International Space Station, Phys. Rev. Lett. **114**, 171103 (2015).
[54] M. Aguilar *et al.* (AMS Collaboration), Precision Measurement of the Helium Flux in Primary Cosmic Rays of Rigidities 1.9 GV to 3 TV with the Alpha Magnetic Spectrometer on the International Space Station, Phys. Rev. Lett. **115**, 211101 (2015).
[55] M. Korsmeier and A. Cuoco, Galactic cosmic-ray propagation in the light of AMS-02: I. Analysis of protons, helium, and antiprotons, Phys. Rev. D **94**, 123019 (2016).
[56] A. W. Strong, I. V. Moskalenko, and O. Reimer, Diffuse continuum gamma rays from the galaxy, Astrophys. J. **537**, 763 (2000).
[57] O. Adriani *et al.* (PAMELA Collaboration), PAMELA measurements of cosmic-ray proton and helium spectra, Science **332**, 69 (2011).
[58] L. C. Tan and L. K. Ng, Parametrisation of hadron inclusive cross sections in p-p collisions extended to very low energies, J. Phys. G **9**, 1289 (1983).
[59] R. P. Duperray, C.-Y. Huang, K. V. Protasov, and M. Buénerd, Parametrization of the antiproton inclusive production cross section on nuclei, Phys. Rev. D **68**, 094017 (2003).
[60] R. Kappl and M. W. Winkler, The cosmic ray antiproton background for AMS-02, J. Cosmol. Astropart. Phys. 9 (2014) 051.
[61] M. de Mauro, F. Donato, A. Goudelis, and P. D. Serpico, New evaluation of the antiproton production cross section for cosmic ray studies, Phys. Rev. D **90**, 085017 (2014).
[62] T. Delahaye, R. Lineros, F. Donato, N. Fornengo, J. Lavalle, P. Salati, and R. Taillet, Galactic secondary positron flux at the Earth, Astron. Astrophys. **501**, 821 (2009).
[63] M. Mori, Nuclear enhancement factor in calculation of Galactic diffuse gamma-rays: A new estimate with DPMJET-3, Astropart. Phys. **31**, 341 (2009).
[64] M. Cirelli, G. Corcella, A. Hektor, G. Hütsi, M. Kadastik, P. Panci, M. Raidal, F. Sala, and A. Strumia, PPPC 4 DM ID: a poor particle physicist cookbook for dark matter indirect detection, J. Cosmol. Astropart. Phys. 3 (2011) 051.
[65] P. Ciafaloni, D. Comelli, A. Riotto, F. Sala, A. Strumia, and A. Urbano, Weak corrections are relevant for dark matter indirect detection, J. Cosmol. Astropart. Phys. 3 (2011) 019.
[66] J. F. Navarro, E. Hayashi, C. Power, A. R. Jenkins, C. S. Frenk, S. D. M. White, V. Springel, J. Stadel, and T. R. Quinn, The inner structure of ΛCDM haloes—III. Universality and asymptotic slopes, Mon. Not. R. Astron. Soc. **349**, 1039 (2004).
[67] D. Merritt, A. W. Graham, B. Moore, J. Diemand, and B. Terzić, Empirical models for dark matter halos. I. Nonparametric construction of density profiles and comparison with parametric models, Astron. J. **132**, 2685 (2006).
[68] J. Einasto, Dark matter, arXiv:0901.0632.
[69] J. F. Navarro, A. Ludlow, V. Springel, J. Wang, M. Vogelsberger, S. D. M. White, A. Jenkins, C. S. Frenk, and A. Helmi, The diversity and similarity of simulated cold dark matter haloes, Mon. Not. R. Astron. Soc. **402**, 21 (2010).

[70] R. Catena and P. Ullio, A novel determination of the local dark matter density, J. Cosmol. Astropart. Phys. 8 (2010) 004.
[71] M. Weber and W. de Boer, Determination of the local dark matter density in our Galaxy, Astron. Astrophys. **509**, A25 (2010).
[72] P. Salucci, F. Nesti, G. Gentile, and C. F. Martins, The dark matter density at the Sun's location, Astron. Astrophys. **523**, A83 (2010).
[73] M. Pato, O. Agertz, G. Bertone, B. Moore, and R. Teyssier, Systematic uncertainties in the determination of the local dark matter density, Phys. Rev. D **82**, 023531 (2010).
[74] F. Iocco, M. Pato, G. Bertone, and P. Jetzer, Dark Matter distribution in the Milky Way: Microlensing and dynamical constraints, J. Cosmol. Astropart. Phys. 11 (2011) 029.
[75] L. J. Gleeson and W. I. Axford, Solar modulation of galactic cosmic rays, Astrophys. J. **154**, 1011 (1968).
[76] C. Evoli, D. Gaggero, D. Grasso, and L. Maccione, Cosmic ray nuclei, antiprotons and gamma rays in the galaxy: a new diffusion model, J. Cosmol. Astropart. Phys. 10 (2008) 018.
[77] G. Jóhannesson, R. R. de Austri, A. C. Vincent, I. V. Moskalenko, E. Orlando, T. A. Porter, A. W. Strong, R. Trotta, F. Feroz, P. Graff, and M. P. Hobson, Bayesian analysis of cosmic ray propagation: evidence against homogeneous diffusion, Astrophys. J. **824**, 16 (2016).
[78] J. Goodman and J. Weare, Ensemble samplers with affine invariance, Commun. Appl. Math. Comput. Sci. **5**, 65 (2010).
[79] D. Foreman-Mackey, D. W. Hogg, D. Lang, and J. Goodman, EMCEE: The MCMC Hammer, Publ. Astron. Soc. Pac. **125**, 306 (2013).
[80] M. Aguilar *et al.* (AMS Collaboration), Antiproton Flux, Antiproton-to-Proton Flux Ratio, and Properties of Elementary Particle Fluxes in Primary Cosmic Rays Measured with the Alpha Magnetic Spectrometer on the International Space Station, Phys. Rev. Lett. **117**, 091103 (2016).
[81] N. Tomassetti, Origin of the cosmic-ray spectral hardening, Astrophys. J. Lett. **752**, L13 (2012).
[82] N. Tomassetti, Cosmic-ray protons, nuclei, electrons, and antiparticles under a two-halo scenario of diffusive propagation, Phys. Rev. D **92**, 081301 (2015).
[83] J. Feng, N. Tomassetti, and A. Oliva, Bayesian analysis of spatial-dependent cosmic-ray propagation: Astrophysical background of antiprotons and positrons, Phys. Rev. D **94**, 123007 (2016).
[84] Y. Génolini, P. D. Serpico, M. Boudaud, S. Caroff, V. Poulin, L. Derome, J. Lavalle, D. Maurin, V. Poireau, S. Rosier, P. Salati, and M. Vecchi, Indications for a High-Rigidity Break in the Cosmic-Ray Diffusion Coefficient, Phys. Rev. Lett. **119**, 241101 (2017).
[85] P. Blasi, On the spectrum of stable secondary nuclei in cosmic rays, Mon. Not. R. Astron. Soc. **471**, 1662 (2017).
[86] A. Reinert and M. W. Winkler, A precision search for WIMPs with charged cosmic rays, J. Cosmol. Astropart. Phys. 1 (2018) 055.
[87] S. P. Reynolds, Filamentary structure in Crab-like supernova remnants, Astrophys. J. **327**, 853 (1988).
[88] D. J. Thompson *et al.*, EGRET high-energy gamma-ray pulsar studies. 1: Young spin-powered pulsars, Astrophys. J. **436**, 229 (1994).
[89] J. M. Fierro *et al.*, EGRET high-energy gamma-ray pulsar studies. II. Individual millisecond pulsars, Astrophys. J. **447**, 807 (1995).
[90] G. Jungman, M. Kamionkowski, and K. Griest, Supersymmetric dark matter, Phys. Rep. **267**, 195 (1996).
[91] W. Chao, H.-K. Guo, H.-L. Li, and J. Shu, Electron flavored dark matter, arXiv:1712.00037.
[92] M. Ackermann *et al.* (Fermi-LAT), Constraining Dark Matter Models from a Combined Analysis of Milky Way Satellites with the Fermi Large Area Telescope, Phys. Rev. Lett. **107**, 241302 (2011).
[93] A. Geringer-Sameth and S. M. Koushiappas, Exclusion of Canonical WIMPs by the Joint Analysis of Milky Way Dwarfs with Fermi, Phys. Rev. Lett. **107**, 241303 (2011).
[94] Y.-L. S. Tsai, Q. Yuan, and X. Huang, A generic method to constrain the dark matter model parameters from Fermi observations of dwarf spheroids, J. Cosmol. Astropart. Phys. 03 (2013) 018.
[95] M. Ackermann *et al.* (Fermi-LAT), Searching for Dark Matter Annihilation from Milky Way Dwarf Spheroidal Galaxies with Six Years of Fermi Large Area Telescope Data, Phys. Rev. Lett. **115**, 231301 (2015).
[96] Shang Li, Yun-Feng Liang, Kai-Kai Duan, Zhao-Qiang Shen, Xiaoyuan Huang, Xiang Li, Yi-Zhong Fan, Neng-Hui Liao, Lei Feng, and Jin Chang, Search for gamma-ray emission from eight dwarf spheroidal galaxy candidates discovered in Year Two of Dark Energy Survey with Fermi-LAT data, Phys. Rev. D **93**, 043518 (2016).
[97] P. A. R. Ade *et al.* (Planck), Planck 2015 results. XIII. Cosmological parameters, Astron. Astrophys. **594**, A13 (2016).
[98] D. Feldman, Z. Liu, and P. Nath, PAMELA positron excess as a signal from the hidden sector, Phys. Rev. D **79**, 063509 (2009).
[99] M. Ibe, H. Murayama, and T. T. Yanagida, Breit-Wigner enhancement of dark matter annihilation, Phys. Rev. D **79**, 095009 (2009).
[100] W.-L. Guo and Y.-L. Wu, Enhancement of dark matter annihilation via Breit-Wigner resonance, Phys. Rev. D **79**, 055012 (2009).
[101] X.-J. Bi, X.-G. He, and Q. Yuan, Parameters in a class of leptophilic models from PAMELA, ATIC and FERMI, Phys. Lett. B **678**, 168 (2009).
[102] X.-J. Bi, P.-F. Yin, and Q. Yuan, Breit-Wigner enhancement considering the dark matter kinetic decoupling, Phys. Rev. D **85**, 043526 (2012).
[103] J. Hisano, M. Kawasaki, K. Kohri, T. Moroi, K. Nakayama, and T. Sekiguchi, Cosmological constraints on dark matter models with velocity-dependent annihilation cross section, Phys. Rev. D **83**, 123511 (2011).
[104] Y. Bai, J. Berger, and S. Lu, Supersymmetric resonant dark matter: A thermal model for the AMS-02 positron excess, arXiv:1706.09974.
[105] Q.-F. Xiang, X.-J. Bi, S.-J. Lin, and P.-F. Yin, A dark matter model that reconciles tensions between the cosmic-ray $e^{\pm}$ excess and the gamma-ray and CMB constraints, Phys. Lett. B **773**, 448 (2017).

[106] J.-S. Niu, T. Li, and F.-Z. Xu, The simple and natural interpretations of the DAMPE cosmic ray electron/positron spectrum within two sigma deviations, arXiv:1712.09586.
[107] J. M. Clem, D. P. Clements, J. Esposito, P. Evenson, D. Huber, J. L'Heureux, P. Meyer, and C. Constantin, Solar modulation of cosmic electrons, Astrophys. J. **464**, 507 (1996).
[108] G. Boella, M. Gervasi, S. Mariani, P. G. Rancoita, and I. G. Usoskin, Evidence for charge drift modulation at intermediate solar activity from the flux variation of protons and α particles, J. Geophys. Res. **106**, 29355 (2001).
[109] I. G. Usoskin, G. A. Bazilevskaya, and G. A. Kovaltsov, Solar modulation parameter for cosmic rays since 1936 reconstructed from ground-based neutron monitors and ionization chambers, J. Geophys. Res. **116**, n/a (2011).
[110] C. Corti, V. Bindi, C. Consolandi, and K. Whitman, Solar modulation of the local interstellar spectrum with Voyager 1, AMS-02, PAMELA, and BESS, Astrophys. J. **829**, 8 (2016).
[111] S.-J. Lin, X.-J. Bi, J. Feng, P.-F. Yin, and Z.-H. Yu, Systematic study on the cosmic ray antiproton flux, Phys. Rev. D **96**, 123010 (2017).
[112] T. Kamae, T. Abe, and T. Koi, Diffractive interaction and scaling violation in $pp \to \pi^0$ interaction and GeV excess in galactic diffuse gamma-ray spectrum of EGRET, Astrophys. J. **620**, 244 (2005).
[113] T. Kamae, N. Karlsson, T. Mizuno, T. Abe, and T. Koi, Parameterization of γ, e^{pm} and neutrino spectra produced by p-p interaction in astronomical environment, Astrophys. J. **647**, 692 (2006); Erratum, Astrophys. J. **662**, 779(E) (2007)].
[114] C. Evoli, D. Gaggero, A. Vittino, M. D. Mauro, D. Grasso, and M. N. Mazziotta, Cosmic-ray propagation with DRAGON2: II. Nuclear interactions with the interstellar gas, arXiv:1711.09616.
[115] R. Jeannerot, X. Zhang, and R. Brandenberger, Nonthermal production of neutralino cold dark matter from cosmic string decays, J. High Energy Phys. 12 (1999) 003.
[116] W. B. Lin, D. H. Huang, X. Zhang, and R. Brandenberger, Nonthermal Production of Weakly Interacting Massive Particles and the Subgalactic Structure of the Universe, Phys. Rev. Lett. **86**, 954 (2001).
[117] Q. Yuan, Y. Cao, J. Liu, P.-F. Yin, L. Gao, X.-J. Bi, and X. Zhang, Gamma rays from warm WIMP dark matter annihilation, Phys. Rev. D **86**, 103531 (2012).
[118] A. Sommerfeld, Über die Beugung und Bremsung der Elektronen, Ann. Phys. (Berlin) **403**, 257 (1931).
[119] J. Hisano, S. Matsumoto, M. M. Nojiri, and O. Saito, Nonperturbative effect on dark matter annihilation and gamma ray signature from the galactic center, Phys. Rev. D **71**, 063528 (2005).
[120] N. Arkani-Hamed, D. P. Finkbeiner, T. R. Slatyer, and N. Weiner, A theory of dark matter, Phys. Rev. D **79**, 015014 (2009).
[121] K. Griest and D. Seckel, Three exceptions in the calculation of relic abundances, Phys. Rev. D **43**, 3191 (1991).
[122] P. Gondolo and G. Gelmini, Cosmic abundances of stable particles: Improved analysis, Nucl. Phys. **B360**, 145 (1991).
[123] H.-B. Jin, B. Yue, X. Zhang, and X. Chen, Cosmic ray e^+e^- spectrum excess and peak feature observed by the DAMPE experiment from dark matter, arXiv:1712.00362.
[124] X.-J. Huang, Y.-L. Wu, W.-H. Zhang, and Y.-F. Zhou, Origins of sharp cosmic-ray electron structures and the DAMPE excess, arXiv:1712.00005 [Phys. Rev. D (to be published)].
[125] F. Yang, M. Su, and Y. Zhao, Dark matter annihilation from nearby ultra-compact micro halos to explain the tentative excess at ~14 TeV in DAMPE data, arXiv:1712.01724.
[126] S.-F. Ge and H.-J. He, Flavor structure of the cosmic-ray electron/positron excesses at DAMPE, arXiv:1712.02744.
[127] I. Cholis, T. Karwal, and M. Kamionkowski, Features in the Spectrum of Cosmic-Ray Positrons from Pulsars, arXiv:1712.00011.
[128] J.-S. Niu, T. Li, W. Zong, H.-F. Xue, and Y. Wang, Probing the dark matter-electron interactions via hydrogen-atmosphere pulsating white dwarfs, arXiv:1709.08804.
[129] D. Maurin, F. Melot, and R. Taillet, A database of charged cosmic rays, Astron. Astrophys. **569**, A32 (2014).
[130] D. Foreman-Mackey, W. Vousden, A. Price-Whelan, M. Pitkin, V. Zabalza, G. Ryan, Emily, M. Smith, G. Ashton, K. Cruz, W. Kerzendorf, T. A. Caswell, S. Hoyer, K. Barbary, I. Czekala, D. W. Hogg, and B. J. Brewer, corner.py: corner.py v1.0.2, 2016.